



## Evaluation of startup time for a model contra-rotating pump-turbine in pump-mode

Downloaded from: <https://research.chalmers.se>, 2024-04-19 10:23 UTC

Citation for the original published paper (version of record):

Fahlbeck, J., Nilsson, H., Salehi, S. (2022). Evaluation of startup time for a model contra-rotating pump-turbine in pump-mode. IOP Conference Series: Earth and Environmental Science, 1079(1). <http://dx.doi.org/10.1088/1755-1315/1079/1/012034>

N.B. When citing this work, cite the original published paper.

# Evaluation of startup time for a model contra-rotating pump-turbine in pump-mode

J Fahlbeck , H Nilsson  and S Salehi 

Department of Mechanics and Maritime Sciences, Chalmers University of Technology,  
SE-412 96 Gothenburg, Sweden

E-mail: [fahlbeck@chalmers.se](mailto:fahlbeck@chalmers.se)

**Abstract.** A larger part of the electricity is today from intermittent renewable sources of energy. However, the energy production from such sources varies in time. Energy storage is one solution to compensate for this variation. Today pumped hydro storage (PHS) is the most common form of energy storage. Usually, it requires a large head, which limits where it can be built. In the EU project ALPHEUS, PHS technologies for low- to ultra-low heads are explored. One of the concepts is a contra-rotating pump-turbine (CRPT). The behaviour of this design at time-varying load conditions is today scarce. In the present work, the impact of the startup time for a CRPT is analysed through computational fluid dynamics (CFD) simulations. The analysis includes a comparison between a coarse and a fine CFD model. The coarse model produces acceptable results and is 50 times cheaper, this model is thus used to assess the startup time. It is found that longer startup times generate lesser loads and peak values. A startup time of 10 s may be a sufficient alternative as the peak loads are heavily reduced compared to faster startups. Furthermore, there is not much difference between a startup time of 20–30 s.

## 1. Introduction

In the *Climate Change 2021* IPCC report [1], it is made abundantly clear that the temperature on the planet is increasing and that human activities are the main cause of this. It is further stated that the temperature will continue to increase to drastic levels if we do not act. One of the cornerstones to prevent this is to decrease the usage of fossil fuels and increase renewable sources for the production of electrical energy [2]. Thus creating an emission neutral electric energy system based on renewable energy sources. Besides hydropower, wind and solar are deemed as the most prominent solutions for emission free energy production. The problem with such renewables is however that they can only produce energy when nature allows it, and to a varying extent. Hence, to have a fully renewable energy system it must be possible to store the energy generated by intermittent renewable energy sources to cope with variations in the energy production. One of the most cost-efficient alternatives to store energy on a large scale is today with pumped hydro storage (PHS) [3].

Traditionally PHS requires a high head to be a viable option, which puts topographical constraints on where it can be built [4]. However, the EU Horizon 2020 project ALPHEUS [5] has the aim to develop PHS for low to ultra-low heads, thus enabling PHS to sites with less favourable topography. One of the technologies explored in the ALPHEUS project is a novel shaft driven (SD) contra-rotating pump-turbine (CRPT) design, which is also the subject of this present study. In the ALPHEUS project, an initial design of a SD-CRPT has earlier been



numerically analysed by Fahlbeck et al. [6] at both steady-state and unsteady-state conditions. The SD in SD-CRPT is dropped for brevity hereafter.

The concept of using a CRPT in a hydropower context is relatively new and is to the knowledge of the authors not in use anywhere today. It is suggested that compared to a single runner configuration, a CRPT may be of smaller size, have higher efficiency, and wider range of operation with independent speed control of the runners [7, 8]. However, it presents a more complex shaft alignment and intricate rotor-rotor interaction. A number of recent scholars have produced results from numerical models and conducted experimental tests of CRPTs with satisfying results [8, 9, 10, 11, 12]. Many of these studies lack an analysis of how the CRPT behaves at time-varying load conditions and mode switching between pump and turbine. Our recent studies show that the runners of the CRPT can experience rapid and large load variations during shutdown and startup procedures in pump-mode, where the startup seems to be the most crucial [13].

In the present study, the time of a startup sequence in pump-mode is numerically investigated with computational fluid dynamics (CFD) simulations. The numerical framework includes 3D transient CFD simulations with a novel pressure boundary condition in the OpenFOAM-v2012 open-source CFD code. In the startup procedure, a valve is opened and the individual rotational speeds of the two runners are increased. The goal is to find a trade-off between startup time and the loads on the runner blades.

## 2. Methodology and material

The design of the CRPT, operating conditions, and setup of the numerical CFD simulations are presented here.

### 2.1. The contra-rotating pump-turbine

The runner designs and a conceptual mechanical mounting assembly of the CRPT used in this study are shown in Figure 1a. The blade geometries of the two individual runners were designed and optimised in model scale by Advanced Design Technology Ltd. as a part of the ALPHEUS project [14]. The machine was designed for purely axial inflow in both pump and turbine modes. The principle with the CRPT, in pump-mode, is that the upstream Runner 1 swirls the flow, and the downstream Runner 2 de-swirls the flow. The downstream Runner 2 thus makes use of the angular momentum induced to the flow by the upstream Runner 1. At the design point, the CRPT reaches hydraulic efficiencies of 88.5% and 90.3% in pump and turbine modes, respectively. The model scale CRPT has a shroud diameter of 27.6 cm, hub diameter of 12.5 cm, 8 and 7 blades are used for runners 1 and 2, respectively.

The CRPT is here studied in model scale due to experimental tests that are later to be made as a part of the ALPHEUS project in a lab at TU Braunschweig. The test facility consists of two large water tanks (upper and lower) located at different height elevations, these are connected with pipes. In Figure 1a a conceptual design of the mechanical components are shown. The two runners are connected to individual shafts leading through the hub and one of the support-struts via a set of bevel gears. This shaft alignment presents an elegant solution to connect the two shafts from the runners to individual motors/generators. The main drawback with this design is that the size of the bevel gears and shafts are constrained by the size of the hub and support-struts. With the current design, the torque of the bevel gears is not to exceed 250 N·m according to the test facility at TU Braunschweig. Our earlier studies of a similar CRPT showed that large force and torque spikes are to be expected during the startup procedure in pump-mode if not handled with care [13]. These torque spikes can easily exceed the torque at the final operating point and must thus be limited.

## 2.2. Startup sequence

Figure 1b shows the evaluated normalised startup sequence for the CRPT in pump-mode as a function of normalised time of the startup ( $t/t_{\max}$ ). During the sequence, a valve is opened and the two runner rotational speeds are increased from the initial values. This particular startup sequence is chosen since it produces a number of unwanted load peaks for a short startup time of  $t_{\max} = 3$  s. Because of this, the impact of the startup time itself is clearer. Our preliminary studies suggest that it is not sufficient to just speedup the runners with a close valve to avoid load peaks during the pump-mode startup. At the first time step of the evaluated sequence, the flow field is fully developed based on earlier simulations and the net head produced by the CPRT matches the gross head of the test facility, so that the flow rate is close to zero (minimal energy loss during startup). At this stage the valve is almost fully closed and the two runners rotate at 61% of their final rotational speed of 1502 rpm. In the sequence, the valve is first opened, followed by the speedup of Runner 2 (downstream) and finally Runner 1 (upstream).

The valve is of the butterfly type, and it is located downstream of the machine in pump-mode. Based on data from the lab at TU Braunschweig, a minor loss coefficient of the valve at various opening angles is estimated as

$$k_v(\alpha) = \exp(-4.2351 \ln(\alpha) + 18.1149). \quad (1)$$

Here  $\alpha$  is the opening angle in degrees, where  $90^\circ$  is fully open and  $0^\circ$  is fully closed. The valve opening is modelled via the outlet boundary condition, described in Section 2.4.

## 2.3. Numerical properties

Incompressible 3D transient CFD simulations are carried out on the computational domain shown in Figure 1c with the OpenFOAM-v2012 open-source CFD software [15]. The  $k-\omega$  SST SAS turbulence model is employed for closure of the Navier-Stokes equations and to account for turbulence [16]. The SAS modifications to the traditional  $k-\omega$  SST model allow for a local decrease in the turbulent viscosity, meaning that the turbulence is resolved in parts of the computational domain. The two runners rotate individually in the simulations by prescribing a time-varying solid body rotation to the individual runner domains.

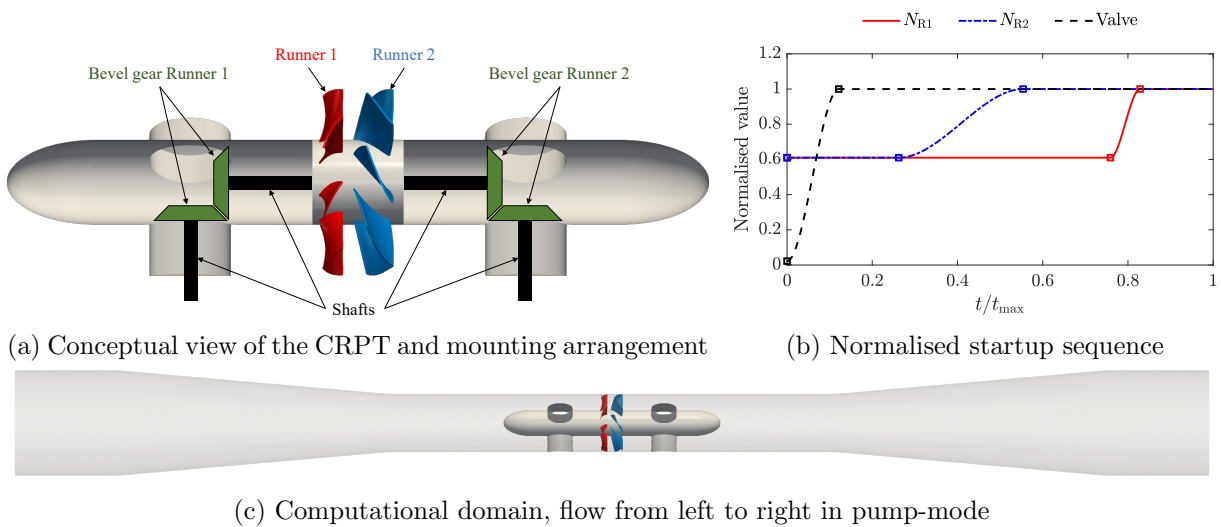


**Figure 1.** Mounting arrangement, evaluated startup sequence and computational domain. Here  $N_{R1}$  and  $N_{R2}$  are the rotational speed of Runner 1 and Runner 2, respectively.

Pressure and velocity is coupled via the PIMPLE algorithm [17]. This combines the PISO [18] and SIMPLE [19] algorithms, using PISO as an inner loop predictor and SIMPLE as an outer loop corrector. The solver algorithm is configured with two inner PISO loops and a maximum of ten outer SIMPLE loops. The outer corrector step is interrupted if convergence is reached within the time step. The PIMPLE algorithm is further configured with one non-orthogonal corrector within every inner loop.

The numerical schemes are of second-order accuracy for all variables, except for convection of turbulent kinetic energy ( $k$ ) and turbulent dissipation rate ( $\omega$ ), where a first-order scheme is used. The convection terms of the momentum equation are handled with the LUST scheme [20]. The time discretisation is made with the second-order backward scheme.

#### 2.4. Boundary conditions

In this study, the flow is driven by the pressure difference of the computational domain. The flow rate is thus part of the solution. The inlet and outlet boundary conditions for pressure is handled with the novel **headLossPressure** boundary condition developed by Fahlbeck et al. [21]. This special boundary condition allows the user to specify the head of the system and it also considers head losses up- and downstream of the computational domain. The result is that the flow-driving pressure difference felt by the pump-turbine is from the system that the CRPT is part of. The boundary condition is set up according to the numbers presented in Table 1, where the minor loss coefficients (except ‘Opening valve’) and surface roughness are according to White [22]. The gross head of the test facility is 6.45 m, which is indicated by the heads specified at the inlet and outlet. For the inlet, only one minor head loss is supplied, and it is a consequence of the flow entering a pipe from the lower reservoir. At the outlet however, there is a bend, a fixed (not used) butterfly valve, and exit effects when the flow enters the upper reservoir. The valve that is part of the startup sequence is located downstream of the computational domain. The valve opening is prescribed as a function of opening angle and time,  $k_v(\alpha, t)$ , according to the sequence shown in Figure 1b. A smallest opening angle of  $\alpha = 2^\circ$  is used for the valve, since the  $k_v$  function of Equation (1) is infinite at  $\alpha = 0^\circ$ . The boundary condition pipe lengths from the computational domain to the lower and upper reservoirs are 1 m and 15.5 m, respectively, as shown in Table 1.

**Table 1.** Input for the pressure boundary condition

	Inlet	Outlet	
<b>Head</b>	3.25	9.7	m
<b>Minor losses</b> (loss coefficient)			
Bend	–	0.2	–
Sharp entrance	–	0.45	–
Sharp exit	1	–	–
Fixed valve	–	0.4	–
Opening valve	–	$k_v(\alpha, t)$	–
<b>Friction losses</b>			
Pipe length	1	15.5	m
Surface roughness	0.05	0.05	mm

The **pressureInletOutletVelocity** boundary condition is used for the velocity at both the inlet and outlet. It is a zero-gradient (homogeneous Neumann) condition for both outflow and inflow, however with a restriction that incoming velocities are normal to each boundary face. The walls are treated with a no-slip condition.

### 2.5. Computational models

Two computational models are used in this study. One fine high-fidelity (HiFi) model with roughly  $10 \times 10^6$  mesh cells, and a coarse low-fidelity (LoFi) model with  $1 \times 10^6$  mesh cells. Both use the computational domain shown in Figure 1c. The time step is  $5 \times 10^{-5}$  s and  $2.5 \times 10^{-4}$  s for the HiFi and LoFi models, respectively. This yields that the LoFi model is at least 50 times less computationally demanding than the HiFi model. As this study concerns long transient CFD simulations, a low computational cost is desirable. The ambition is that the LoFi model should be able to capture the major features of the flow.

The computed pump power, discharge, net head, and hydraulic efficiency at the chosen final operating point for the HiFi and LoFi models are presented in Table 2. Note that this operating point is not the same as the design point. The LoFi model under-predicts the performance slightly compared to the HiFi model, but it is deemed as acceptable given the much lower computational cost.

**Table 2.** Computed engineering properties for the HiFi and LoFi models

	HiFi	LoFi	Difference
<b>Power</b> (kW)	62.0	59.9	3.4%
<b>Discharge</b> (l/s)	488.3	462.0	5.4%
<b>Net head</b> (m)	11.0	11.0	0.0%
<b>Hydraulic efficiency</b> <sup>a</sup> (%)	84.8	82.9	–

<sup>a</sup> The efficiency is based on the net head of the CRPT

## 3. Results and discussion

Results from a startup sequence of 3 s for the HiFi and LoFi models are first presented. Thereafter, results are presented from sequences where the startup time is varied between 3 to 30 s. Recall the startup sequence shown in Figure 1b as this is central for the discussion. Axial force and torque variations are primarily focused on in this study. The forces and torques are from integrated normal and shear stresses on the runner blade surfaces, and the flow rate is from integrating the volumetric face flux at the inlet. All the quantities shown in the graphs are smoothed, thus only the main variation is analysed.

### 3.1. Part I: Comparison of HiFi and LoFi models during a 3 s startup

The analysis starts by considering a startup sequence where the time of the startup is 3 s ( $t_{\max}$ ). At this stage the LoFi model is compared to the HiFi model, see Section 2.5 for further details. The motivation is to get an understanding of how the two models correlate with one another. In Figure 2 the computed flow rate, axial forces, and torques of the two models are shown. The first to notice is that the opening of the valve has a limited effect on all quantities. This is explained by the initial rotational speed of the runners being set so that the net head of the CRPT equals the gross head of the system. This results in a negligible flow through the system, which is shown in Figure 2a. In fact, the flow starts to change first when the rotational speed of Runner 2 starts to increase. The discharge of the HiFi and LoFi models are until  $t/t_{\max} \approx 0.45$  rather similar. However, after this the models start to deviate. Similar phenomena are occurring for the force and torque of Runner 2, as shown in Figures 2d and 2e, respectively. The HiFi model more quickly reaches the flow rate plateau before the Runner 1 rotational speed is increased. This is plausibly explained by the fact that the HiFi model resolves a larger part of the boundary layer since the average  $y^+$  in the runner domains are 31 and 137 for the HiFi and LoFi models,

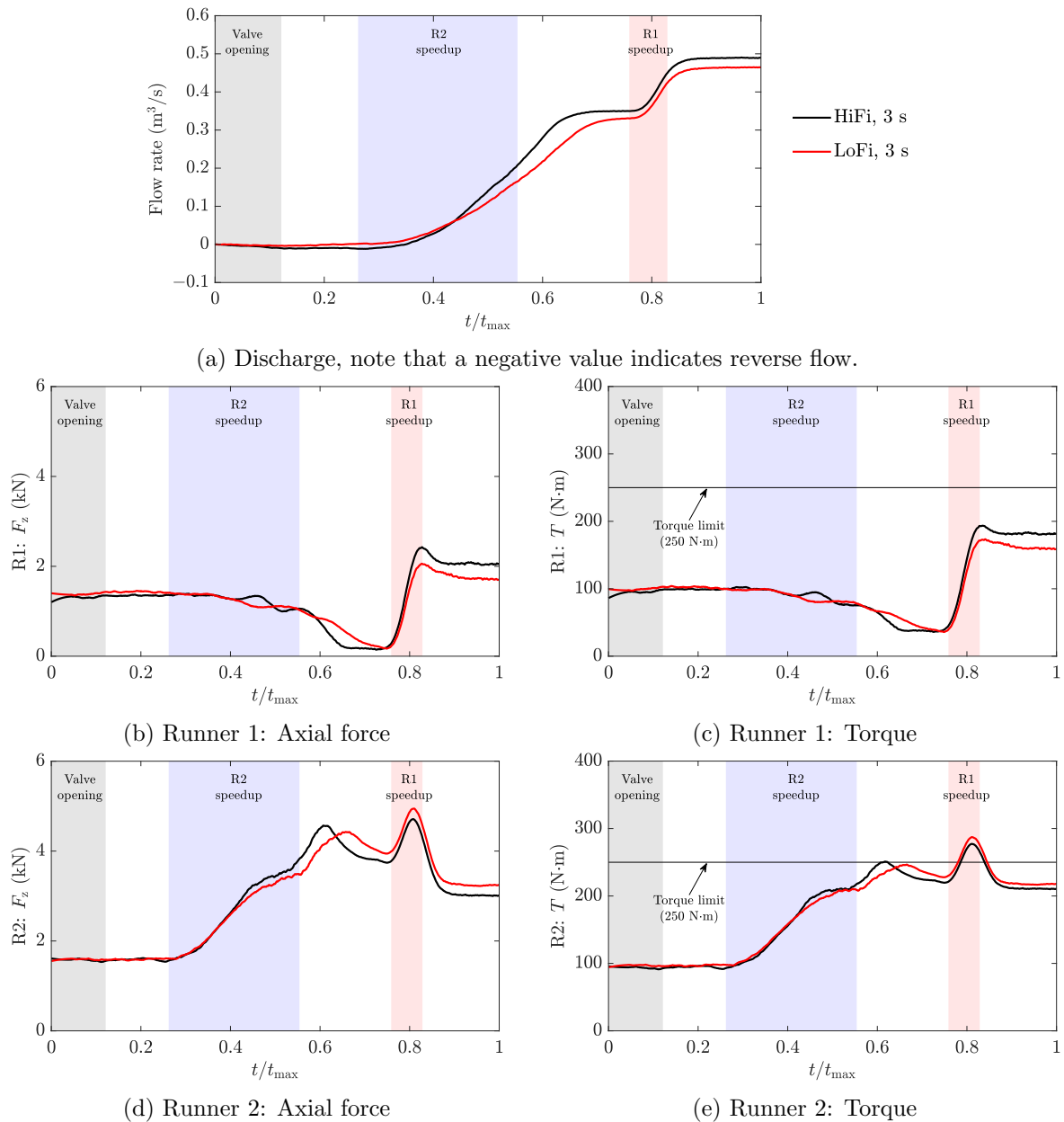


**Figure 2.** Computed flow rate, axial forces, and torques as a function of normalised time for the HiFi and LoFi models with  $t_{\max} = 3$  s. The coloured areas of grey, blue, and red indicate the valve opening, speedup of Runner 2 and Runner 1, respectively.

respectively, at the final time step. The lower  $y^+$  value of the HiFi model suggests a more realistic momentum transfer between runners and flow, compared to the LoFi model. When the rotational speed of Runner 1 starts to increase, the shape of the flow rate curves are similar between the HiFi and LoFi models. It is evident in both cases that there are hysteresis effects in the flow, this is because the flow rate continues to increase after the runners have reached their final speeds.

The general trends for the loads on Runner 1, shown in Figures 2b and 2c, are adequately captured by the LoFi model. Some offset is noted between the speedup of the runners

( $0.55 < t/t_{\max} < 0.75$ ), and after Runner 1 has reached its final rotational speed. The time of the peak axial force and torque at  $t/t_{\max} \approx 0.83$  is captured by both models, showing that the LoFi model manages to predict where a peak may be expected.

Figures 2d and 2e show the axial force and torque of Runner 2, respectively. The location of the maximum axial force and torque ( $t/t_{\max} \approx 0.80$ ) for Runner 2 is predicted to occur at the same time and at similar magnitudes for the two models. However, the maximum allowed torque of 250 N·m from the lab is at this time exceeded. The peak at  $t/t_{\max} \approx 0.60$  for HiFi and at  $t/t_{\max} \approx 0.65$  for the LoFi, is less well captured by the LoFi model. The delay of the peak seems to be correlated with the lagging of the flow rate for the LoFi model.

Another observation for the loads between Runner 1 (Figures 2b and 2c) and Runner 2 (Figures 2d and 2e), is that the peak values appearing as Runner 1 is accelerated first occur at the downstream Runner 2 and later at the upstream Runner 1. An explanation to the peak loads on Runner 2 is as follows; when the rotational speed of Runner 1 is increased; flow rate is being rapidly accelerated and flow is pushed towards Runner 2; generating a large impulse on the runner, before it has had time to appropriately accommodate to the higher flow rate. The peak loads on Runner 2 is thus a direct effect of the acceleration in the rotational speed of Runner 1. The load peak for Runner 1 is also caused by the rapid acceleration in rotational speed, which adds more momentum into the flow. It takes some time after the Runner 1 acceleration before the loads on the runners stabilise and reach steady conditions due to hysteresis.

The LoFi model is able to capture the general trends to an acceptable level, which is the purpose of the model. In Section 2.5 it was mentioned that the LoFi is at least 50 times faster to run than the HiFi model. The HiFi model was run with 384 cores and required just over  $50 \times 10^3$  core hours in total, whereas only 32 cores were used for the LoFi model at roughly  $1 \times 10^3$  core hours. This yields that the LoFi model indeed is 50 times faster than the HiFi model for the evaluated startup sequence. Despite the shortcomings of the LoFi model, it is deemed adequate enough to proceed with the evaluation of the startup time.

### 3.2. Part II: Effects of startup time with the LoFi model

In this second part of the results, the effects of the startup time ( $t_{\max}$ ) is analysed with the LoFi model. Figure 3 shows the flow rate through the domain and loads on Runner 2 at various startup times, from 3 s to 30 s. As noted in Section 3.1, the loads on Runner 1 are less than on Runner 2. Loads are thus only analysed for Runner 2 in this part. A rough general observation is that by a longer startup time, the various quantities have a less drastic behaviour and lower peak values. Already by increasing  $t_{\max}$  from 3 to 6 s much is gained. However, the effects between  $t_{\max}$  of 20 and 30 s are less obvious. The flow rate, shown in Figure 3a, clearly indicate hysteresis effects by a faster startup scheme. This is because, with a longer startup time, the flow rate is accelerated as the runners increase their rotational speed. With a fast startup ( $t_{\max} = 3$  s), the flow rate continues to increase even as the rotational speed of the runners do not change.

The variation in axial force and torque for Runner 2 are shown in Figures 3b and 3c, respectively. The general appearance of the two quantities is rather similar. The first load increase is caused by the speedup of Runner 2 rotational speed. A load spike arises as the flow rate approaches its plateau value. An explanation to the increase in loads is that, as the rotational speed of Runner 2 is increased, angular momentum is added to the flow, which in turn is realised by an acceleration in flow rate. As the flow rate increases, the axial velocity towards Runner 1 (upstream) is accelerated. However, the rotational speed of this runner is not changed at this stage, resulting in a lower flow angle leaving Runner 1. This means that the flow in front of Runner 2 is ‘under-swirled’, meaning that the relative flow angle upstream of Runner 2 is too small. Thus Runner 2 is for a short period responsible for most of the momentum entering the flow, which is causing the first peak. For a longer startup time, the flow acceleration is less drastic, hence the smaller peak values. The loads recover (except  $t_{\max} = 3$  s) to a plateau as



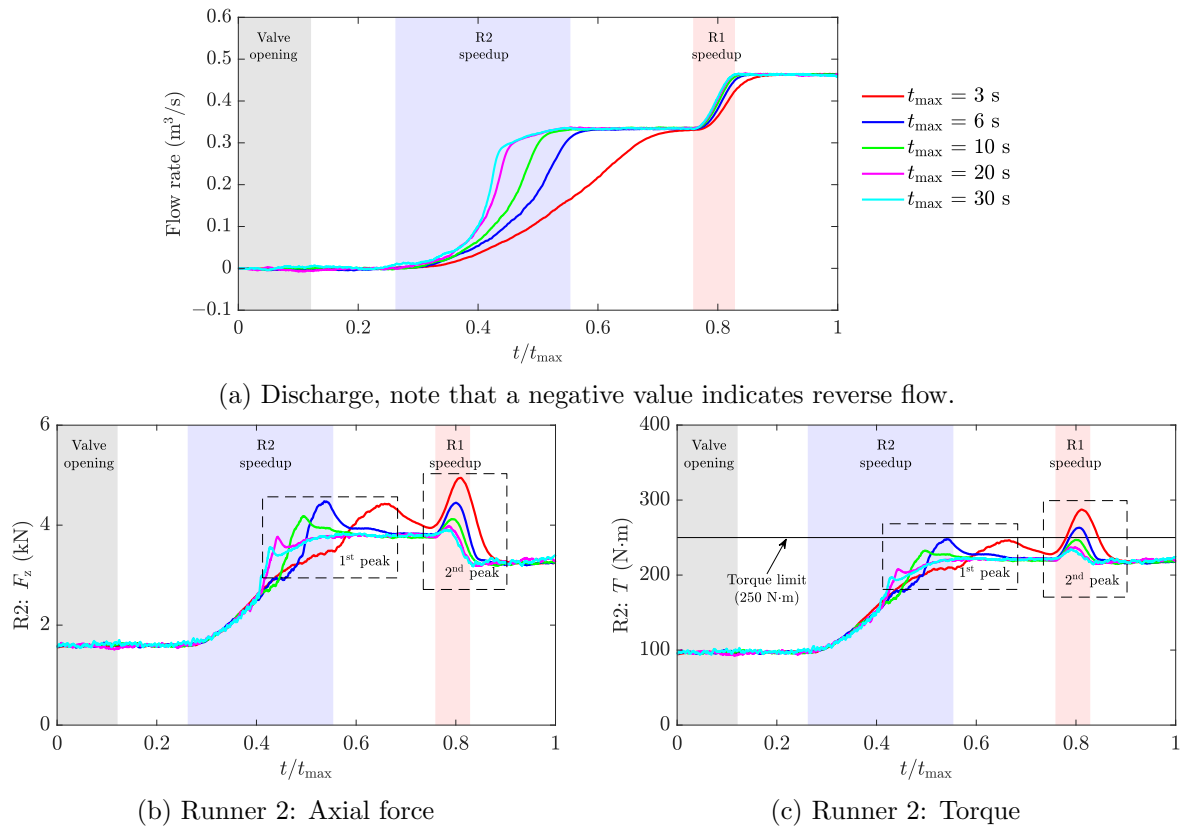


**Figure 3.** Computed flow rate, axial force, and torque for runner 2 as a function of normalised time for various startup times ( $t_{\max}$ ). The coloured areas of grey, blue, and red indicate the valve opening, speedup of Runner 2 and Runner 1, respectively.

the machine has time to adapt to the new rotational speed of Runner 2.

During the speedup of Runner 1, further angular momentum is added into the flow, as indicated in Figure 2c, which accelerates the flow. This means that Runner 1 will push more flow towards Runner 2 and the second load peak appear. At the faster startups, Runner 2 will not have time to adapt to this, resulting in a high impulse and thus loads, as discussed in Section 3.1. However, as shown in Figure 3c, the maximum allowed torque is not surpassed by the relatively fast startup time of 10 s. A faster startup than this will result in the maximum allowed torque being exceeded. A slower startup is of course feasible from a load perspective, but a fast startup is nonetheless desirable as this gives a more flexible machine.

Figure 4 shows contours of tangential velocity and vectors of secondary flow at a plane located just downstream of Runner 2. At the time step  $t/t_{\max} = 0.766$  (prior to the second load peak) shown in Figure 4a, there is not much difference in the secondary flow for the different startup times. It is noted that the fastest startup has slightly higher tangential velocity, which is also supported by the higher torque shown in Figure 3c. As the second load peak approaches at  $t/t_{\max} = 0.800$  differences for the startup times becomes clearer, as shown in Figure 4b. From a short to a longer startup, the tangential velocity leaving Runner 2 decreases. However, the vectors show a clear swirl leaving the runners. The direction of the secondary flow vectors and the high tangential velocity show that Runner 2 ‘over-swirls’ the flow, and it is worse for a shorter startup time. After the load peak at  $t/t_{\max} = 0.833$ , shown in Figure 4c, the swirl decays. The tangential velocity is less pronounced for the slow startup time. The vectors also indicate that there is a less prominent swirl remaining at this time step for a slow compared to

a fast startup.

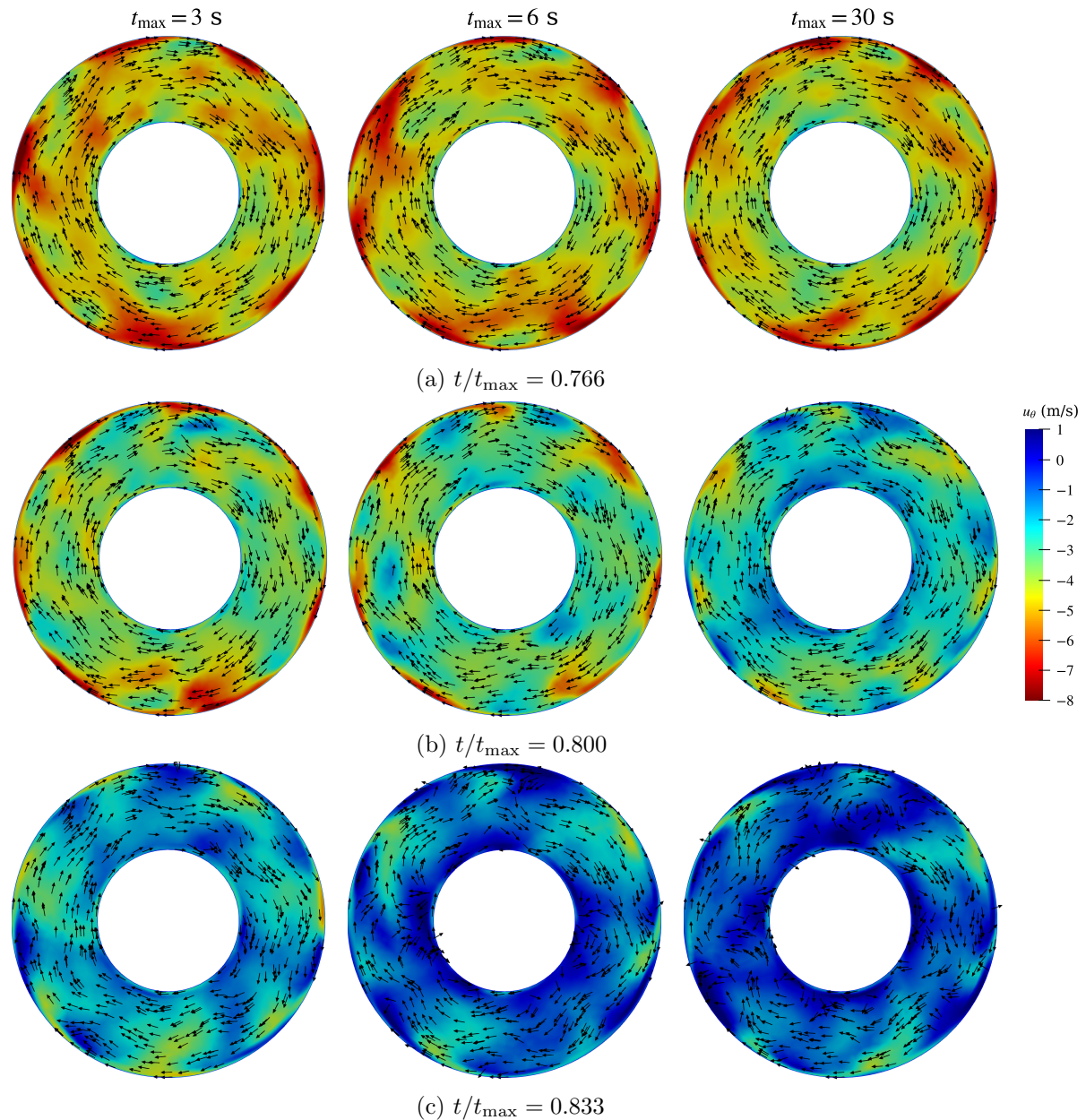


**Figure 4.** Contours of tangential velocity and vectors of secondary flow at a plane downstream of Runner 2 at three time steps. From left to right column  $t_{\max}$  is 3, 6 and 30 s.

#### 4. Conclusions

A fine (HiFi) model and a coarse (LoFi) model are compared on a startup sequence of 3 s to evaluate the usability of the LoFi model. It is established that a LoFi model can capture the majority of the flow features to an acceptable extent when compared with the HiFi model. Since the LoFi model does not resolve as much of the boundary layer as the HiFi model, the load predictions are slightly off compared to the HiFi model. Additionally, it is found that Runner 2

experiences the worst load conditions, whereas Runner 1 has less exaggerated behaviour. The computational cost of the LoFi model is 50 times less than for the HiFi model. Given that the LoFi model could capture the startup adequately and at a much lower computational cost, it is deemed good enough to be used for the main study.

Five startup times, ranging from 3 s to 30 s were examined. With a longer startup time, the load behaviour is less drastic. This is primarily because the runners have time to adapt to changes during the sequence. Already at a startup time of 10 s, the peak loads are largely reduced and the torque is within the prescribed limit from the lab of 250 N·m. It is hence deemed that a 10 s startup time is a reasonable trade-off between the time of the startup and expected loads. The difference in loads for startup times of 20 and 30 s did not differ much. It is thus not much gained by increasing the startup time further. This is because a faster startup is more flexible and a startup time of 10 s should be feasible for the future lab tests if this particular (non-optimised) startup sequence is used.

## Acknowledgement

This project has received funding from the European Union's Horizon 2020 research and innovation programme under grant agreement No. 883553. The computations were enabled by resources provided by the Swedish National Infrastructure for Computing (SNIC) at NSC and C3SE, partially funded by the Swedish Research Council through grant agreement No. 2018-05973.

## References

- [1] IPCC 2021 *Climate Change 2021: The Physical Science Basis. Contribution of Working Group I to the Sixth Assessment Report of the Intergovernmental Panel on Climate Change* (Cambridge University Press)
- [2] IRENA 2020 *Global Renewables Outlook: Energy Transformation 2050* (International Renewable Energy Agency (IRENA)) ISBN 978-92-9260-238-3
- [3] Zakeri B and Syri S 2015 *Renewable and Sustainable Energy Reviews* **42** 569–596 ISSN 1364-0321
- [4] Hoffstaedt J P *et al.* 2022 *Renewable and Sustainable Energy Reviews* **158** 112119 ISSN 1364-0321
- [5] 2022 ALPHEUS H2020 URL <https://alpheus-h2020.eu/> accessed on 13 April 2022
- [6] Fahlbeck J, Nilsson H, Salehi S, Zangeneh M and Joseph M 2021 *IOP Conference Series: Earth and Environmental Science* **774** 012066 ISSN 1755-1315
- [7] Furukawa A, Shigemitsu T and Watanabe S 2007 *Journal of Thermal Science* **16** 7–13 ISSN 1993-033X
- [8] Xiuli W, Bin L, Yang L, Yan Z, Rongsheng Z, Yun L and Qiang F 2020 *Frontiers in Energy Research* **8** ISSN 2296-598X
- [9] Vagnoni E, Andolfatto L, Richard S, Münch-Alligné C and Avellan F 2018 *Renewable Energy* **126** 943–953 ISSN 0960-1481
- [10] R Subbarao and M Govardhan 2020 *Journal of Applied Fluid Mechanics* **13** 767–777 ISSN 1735-3572
- [11] Kim J W, Suh J W, Choi Y S, Lee K Y, Kanemoto T and Kim J H 2018 *International Journal of Rotating Machinery*
- [12] Kim J H, Kasahara R, Kanemoto T, Miyaji T, Choi Y S, Kim J H, Lee K Y and Galal A M 2014 *Advances in Mechanical Engineering* **6** ISSN 1687-8140
- [13] Fahlbeck J, Nilsson H and Salehi S 2021 *Energies* **14** 3593 ISSN 1996-1073
- [14] Melvin J, Fahlbeck J, Mehrdad Z and Nilsson H 2020 Optimized initial down-scaled model design of SD-CRPT D2.1 Public V1.0 EC <https://alpheus-h2020.eu/> available online: [https://alpheus-h2020.eu/wp-content/uploads/2021/01/ALPHEUS\\_Deliverable\\_2.1\\_SD-CRPT\\_V1.0.pdf](https://alpheus-h2020.eu/wp-content/uploads/2021/01/ALPHEUS_Deliverable_2.1_SD-CRPT_V1.0.pdf) accessed on 13 April 2022
- [15] Greenshields C J 2021 *The OpenFOAM Foundation* 241
- [16] Menter F R and Egorov Y 2010 *Flow, Turbulence and Combustion* **85** 113–138 ISSN 1573-1987
- [17] Robertson E, Choudhury V, Bhushan S and Walters D K 2015 *Computers & Fluids* **123** 122–145 ISSN 0045-7930
- [18] Issa R I 1986 *Journal of Computational Physics* **62** 40–65 ISSN 0021-9991
- [19] Patankar S V and Spalding D B 1972 *International Journal of Heat and Mass Transfer* **15** 1787–1806 ISSN 0017-9310
- [20] Weller H 2012 *Monthly Weather Review* **140** 3220–3234 ISSN 1520-0493, 0027-0644
- [21] Fahlbeck J, Nilsson H and Salehi S 2022 *OpenFOAM Journal* **2** 1–12 ISSN 2753-8168
- [22] White F M 2016 *Fluid mechanics*. 8th ed (McGraw-Hill) ISBN 978-981-4720-17-5